LiDAR Strip Adjustment Using Multifeatures Matched With Aerial Images

Yongjun Zhang, Xiaodong Xiong, Maoteng Zheng, and Xu Huang

***Abstract*—Airborne light detecting and ranging (LiDAR) systems have been widely used for the fast acquisition of dense topographic data. Regrettably, coordinate errors always exist in LiDAR-acquired points. The errors are attributable to several sources, such as laser ranging errors, sensor mounting errors, and position and orientation system (POS) systematic errors, among others. LiDAR strip adjustment (LSA) is the solution to eliminating the errors, but most state-of-the-art LSA methods neglect the influence from POS systematic errors by assuming that the POS is precise enough. Unfortunately, many of the LiDAR systems used in China are equipped with a low-precision POS due to cost considerations. Subsequently, POS systematic errors should be also considered in the LSA. This paper presents an aerotriangulation-aided LSA (AT-aided LSA) method whose major task is eliminating position and angular errors of the laser scanner caused by boresight angular errors and POS systematic errors. The aerial images, which cover the same area with LiDAR strips, are aerotriangulated and serve as the reference data for LSA. Two types of conjugate features are adopted as control elements (i.e., the conjugate points matched between the LiDAR intensity images and the aerial images and the conjugate corner features matched between LiDAR point clouds and aerial images). Experiments using the AT-aided LSA method are conducted using a real data set, and a comparison with the three-dimensional similarity transformation (TDST) LSA method is also performed. Experimental results support the feasibility of the proposed AT-aided LSA method and its superiority over the TDST LSA method.**

***Index Terms*—Aerial image, corner feature, image matching, light detecting and ranging (LiDAR) intensity image, LiDAR strip adjustment (LSA).**

I. Introduction

THE airborne light detecting and ranging (LiDAR) system has been playing an increasingly important role in the fast acquisition of topographic data in recent years. The LiDAR data collected by the airborne LiDAR system are useful for many applications, such as orthophoto production, building and road extraction, city analysis, traffic analysis, etc. [1]–[4]. LiDAR is a combination system that includes three units: a laser scanner, a Global Positioning System (GPS), and an inertial measurement unit (IMU). The GPS and IMU constitute the position and orientation system (POS), which measures the position and attitude value of the LiDAR system. Elaborate descriptions of airborne LiDAR systems can be found in [5] and [6]. Airborne LiDAR data collection is usually conducted in a stripwise pattern, and the LiDAR point clouds obtained during one flight strip is called a LiDAR strip. Due to its character as a combined system, apart from some random errors, the coordinates of LiDAR strip points also suffer from many systematic errors. According to past research, the major systematic errors include laser ranging errors, mirror angle scale errors, mounting errors (lever arm bias errors and boresight angular errors), and POS systematic errors [5], [7]–[10]. These system errors result in discrepancies between overlapping LiDAR strips and between the LiDAR strip and the ground truth.

With the purpose of eliminating these discrepancies, various LiDAR strip adjustment (LSA) methods have been proposed in the past, and the existing approaches can be classified into data-driven methods and sensor system-driven methods [7], [8], [11], [12]. Data-driven methods apply translation and rotation models in LSA [e.g., a six-parameter rigid body transformation (three shifts and three rotations)] or even a simple vertical shift. Some methods are concerned only with the elimination of vertical discrepancies [12], [13]. Apparently, they are only effective for the data of relatively flat terrain. Other methods with the ability to correct both planimetric and vertical discrepancies have been proposed by adopting the translation and rotation models [8], [9], [11], [14], [15]. Due to the combined nonlinear effects of various systematic errors, the consequential distortion of LiDAR strips cannot be simply assumed as linear [7], [16]. Hence, the adoption of linear models, such as translation and rotation, cannot eliminate the discrepancies completely, and rigorous sensor-system-driven approaches are required. Sensor-system-driven methods adopt LiDAR geolocation equations as adjustment models. These methods require the original observations (GPS, IMU, and laser scanner measurements) or at least the trajectory and the time-tagged point clouds [7], [10]. Most sensor-system-driven methods only calibrate the systematic errors of the mounting parameters and ranging [7], [10], [17]–[23], based on the fact that the state-of-the-art GPS/IMU on board possesses sufficient precision and that the POS systematic errors therefore are negligible. However, mainly due to the high cost of such state-of-the-art systems, many of the LiDAR systems used in China are equipped with low-precision POS. If other possible negative factors are considered, such as weak GPS constellation geometry, inadequate reference GPS stations, and even limited professional ability to conduct GPS/IMU data postprocessing, the POS systematic errors experienced can be very large in magnitude and will also be the major error source of LiDAR strip distortion. Accurate

Manuscript received September 10, 2013; revised March 9, 2014 and April 16, 2014; accepted June 3, 2014. Date of publication July 8, 2014; date of current version August 12, 2014. This work was supported in part by the National Natural Science Foundation of China under Grant 41171292 and Grant 41322010, by the National Basic Research Program of China (973 Program) under Grant 2012CB719904, by the China Scholarship Council, by the Fundamental Research Funds for the Central Universities under Grant 2012213020207, and by the Academic Award for Excellent Ph.D. Candidates funded by the Ministry of Education of China under Grant 5052012213001.

The authors are with the School of Remote Sensing and Information Engineering, Wuhan University, Wuhan 430079, China (e-mail: zhangyj@whu.edu.cn; yongjun_zhang@sina.com).

Color versions of one or more of the figures in this paper are available online at http://ieeexplore.ieee.org.

Digital Object Identifier 10.1109/TGRS.2014.2331234

calibration of POS systematic errors therefore becomes very essential for LSA under these circumstances.

Both data-driven and sensor-system-driven methods require control elements or tie elements. The control or tie elements currently used in the estimation and correction of strip discrepancies are mainly line and surface features [7]–[11], [14], [16]–[18], [20]–[22], [24]–[26]. For the extraction of these features, sophisticated or sometimes manually interacted procedures are employed, such as LiDAR point segmentation, plane or surface extraction, and plane intersection. Because the field of view of LiDAR is narrower than a digital camera and the side distance of adjacent flight lines generally is planed according to the side overlap of aerial images, the side overlap of adjacent LiDAR strips is usually very small. When man-made objects are rare, only a small number of tie elements (e.g., line or planar features) can be matched between adjacent LiDAR strips. The insufficient tie elements usually lead to unreliable LSA results. If absolute adjustment with the purpose of reducing the discrepancies between the LiDAR strips and the ground truth is required, LiDAR-specific ground control targets (L-SGCTs) should be placed. The L-SGCTs must be large enough and only can be installed before the flight mission. As the overlaps of LiDAR strips usually fluctuate, some targets may be missed from LiDAR strips [27]. Considering the aforementioned aspects, an effective, convenient, and economical method to obtain tie and control elements for LSA is urgently needed.

Nowadays, many LiDAR systems are equipped with high-resolution digital cameras, which can obtain high-resolution digital imagery simultaneously during the collection of LiDAR strips. If a few photogrammetry-specific ground control points (P-SGCPs) are measured, POS-aided aerotriangulation can be conducted to obtain the precise exterior orientation parameters of aerial images [28], [29]. Unlike the L-SGCTs, the P-SGCPs need not be specially manufactured and can be measured after the flight mission, and their optimum positions can be determined by checking the real overlap of the aerial images. The measurement of P-SGCPs is therefore economical and flexible. Once the aerial images are aerotriangulated, they can provide control information for the LSA by matching the conjugate features between the LiDAR data and the aerial imagery. Conjugate feature matching between aerial images and LiDAR data has been intensively researched to achieve the automatic registration of the two data sets. The features adopted in the registration are mainly straight lines and planar patches [30], [31]. It was commonly believed in the past that the matching of conjugate distinctive points between aerial images and LiDAR point clouds is difficult due to the great difference in the resolutions and imaging mechanisms of the two data sets [30], [32]. However, with the advent of advanced laser scanning devices, intensity signals reflected from ground objects can be precisely measured and recorded. Therefore, high-quality LiDAR intensity images can be generated and matched with aerial images [32], [33].

Based on the given analysis, this paper proposes a sensor-system-driven aerotriangulation-aided LSA (AT-aided LSA) method. Boresight angular errors and POS systematic errors are the main concern of this method and will be eliminated during the LSA. This method needs the following information: time-tagged LiDAR strips, aerial images covering the same area with LiDAR strips, the POS trajectory, mounting parameters used to generate the given LiDAR strips, and a few P-SGCPs. The basic principle of this method is the utilization of aerotriangulated aerial images as the reference data for the LSA by matching the conjugate multifeatures between the aerial images and LiDAR strips. The originality of this paper is as follows. 1) A mathematical model of the AT-aided LSA method is derived from the LiDAR geolocation equation and the LiDAR position/angular error correction models. The errors of POS position/attitude observations as well as the boresight angular errors are corrected in the LSA by fitting these errors with second-order polynomials. 2) The aerotriangulated aerial images are used as reference data in the LSA. Multifeatures are matched between aerial images and LiDAR data and then used as control elements for LSA. Apart from the conjugate distinctive points matched between downsampled aerial images and LiDAR intensity images, the conjugate building corner features between aerial images and LiDAR points are also matched using our previous proposed method.

This paper is organized as follows. In Section II, the mathematical model of the AT-aided LSA method is derived from the LiDAR geolocation equation and the LiDAR position/angular error correction models. Coordinate error correction of LiDAR strips is achieved after the correction of the laser scanner position/angular errors. In Section III, to obtain massive control elements for the LSA, aerial images covering the same area with LiDAR strips are used as the reference data. Photogrammetric aerotriangulation of the aerial images is performed with the assistance of POS data, LiDAR strips, and a few P-SGCPs. Two types of conjugate features are matched, which are the conjugate distinctive points matched between the aerial images and the LiDAR intensity images and the conjugate corner features matched between the irregularly spaced LiDAR point clouds and the aerial images. Then, the control elements needed in LSA are derived from these conjugate features. In Section IV, the workflow of the proposed LSA procedure is presented. In Section V, the performance of the proposed AT-aided LSA method is evaluated using a real data set. For comparison purposes, the traditional three-dimensional similarity transformation (TDST) LSA method is also tested using the same data. In the TDST LSA method, the POS data are not needed; hence, it is a data-driven method. In Section VI, this paper's conclusions and recommendations are presented.

II. Mathematical Model of AT-Aided LSA

The coordinates of laser foot point P in the local reference frame can be derived by the LiDAR geolocation equation [7]–[10], [18]–[22] as follows:

$$\begin{bmatrix} X_P(t) \\ Y_P(t) \\ Z_P(t) \end{bmatrix} = \begin{bmatrix} X_G(t) \\ Y_G(t) \\ Z_G(t) \end{bmatrix} + R_I(t) \begin{bmatrix} X_L \\ Y_L \\ Z_L \end{bmatrix} + R_I(t) R_{MIS\_L} R_R(t) \begin{bmatrix} 0 \\ 0 \\ d(t) \end{bmatrix} \quad (1)$$

where t is the time when point P is obtained, $[X_P(t), Y_P(t), Z_P(t)]$ is the coordinate of point P in the local reference frame at time t, $[X_G(t), Y_G(t), Z_G(t)]$ is the POS position observation value in the local reference frame at time t, $R_I(t)$ is the rotation matrix composed by the POS attitude angular observations in the local reference frame at time t, $[X_L, Y_L, Z_L]$ is the lever arm bias of the laser scanner in the POS body frame, R_{MIS_L} is the rotation matrix of the boresight angles of the laser scanner in the POS body frame, $R_R(t)$ is the rotation matrix of the laser beam angles in the laser scanner frame at time t, and $d(t)$ is the range between the laser fire point and the foot point. For a better understanding of these frames and the transformations, please refer to [8].

The POS and the laser scanner are highly integrated, and there would be periodic calibration for their mounting parameters; hence, during one flight mission, the lever arm bias $[X_L, Y_L, Z_L]$ and the rotation matrix R_{MIS_L} of the boresight angles in (1) are both fixed values, and the lever arm bias errors can be assumed as small. After the manufacturer's calibration, the measurement errors for the range and the laser beam angles of the laser scanner are also small. Hence, the major error sources are boresight angular errors and POS position/angular errors. Previous research has revealed that the POS angular errors, the mounting angular errors, and the scan angle errors of the laser scanning are highly correlated and cannot be separately resolved in the estimation process [10]. Therefore, only one group of position/angular errors is introduced to the LSA in this paper. Moreover, (1) can be simplified as follows:

$$\begin{bmatrix} X_P(t) \\ Y_P(t) \\ Z_P(t) \end{bmatrix} = \begin{bmatrix} X_{\mathrm{LDR}}(t) \\ Y_{\mathrm{LDR}}(t) \\ Z_{\mathrm{LDR}}(t) \end{bmatrix} + R_{\mathrm{LDR}}(t) \begin{bmatrix} X_{\mathrm{PL}}(t) \\ Y_{\mathrm{PL}}(t) \\ Z_{\mathrm{PL}}(t) \end{bmatrix} \tag{2}$$

where $[X_P(t), Y_P(t), Z_P(t)]$ share the same definition in (1); $[X_{\mathrm{LDR}}(t), Y_{\mathrm{LDR}}(t), Z_{\mathrm{LDR}}(t)]$ is the position of laser scanner (GPS measured position corrected for lever arm bias) in the local reference frame

$$\begin{bmatrix} X_{\mathrm{LDR}}(t) \\ Y_{\mathrm{LDR}}(t) \\ Z_{\mathrm{LDR}}(t) \end{bmatrix} = \begin{bmatrix} X_G(t) \\ Y_G(t) \\ Z_G(t) \end{bmatrix} + R_I(t) \begin{bmatrix} X_L \\ Y_L \\ Z_L \end{bmatrix} \tag{3}$$

and $R_{\mathrm{LDR}}(t)$ is the rotation matrix calculated by $(\omega_{\mathrm{LDR}}(t), \varphi_{\mathrm{LDR}}(t), \kappa_{\mathrm{LDR}}(t))$ (the attitude angles of laser scanner derived from IMU measured angles corrected for coarse estimation of boresight angles) in the local reference frame

$$R_{\mathrm{LDR}}(t) = R_I(t) R_{MIS\_L}. \tag{4}$$

$[X_{\mathrm{PL}}(t), Y_{\mathrm{PL}}(t), Z_{\mathrm{PL}}(t)]$ is the coordinate of LiDAR point P in the laser scanner frame at time t, which can be assumed to be without errors based on the given analysis as

$$\begin{bmatrix} X_{\mathrm{PL}}(t) \\ Y_{\mathrm{PL}}(t) \\ Z_{\mathrm{PL}}(t) \end{bmatrix} = R_R(t) \begin{bmatrix} 0 \\ 0 \\ d(t) \end{bmatrix}. \tag{5}$$

Owing to the POS shift/drift errors and boresight angular errors, errors exist in $[X_{\mathrm{LDR}}(t), Y_{\mathrm{LDR}}(t), Z_{\mathrm{LDR}}(t)]$ and $R_{\mathrm{LDR}}(t)$ in (2). In fact, the systematic errors of the position observations and the angular observations of the POS system are time dependent in a single strip [28], and Kager uses time-dependent polynomials to correct POS observation values [34]. Therefore, as is shown in (6), second-order polynomials are adopted to fit the systematic errors of the laser scanner position and angular observations for a short period of time in this paper. Thus

$$\begin{bmatrix} X_{\mathrm{LDR}}(t) \\ Y_{\mathrm{LDR}}(t) \\ Z_{\mathrm{LDR}}(t) \\ \omega_{\mathrm{LDR}}(t) \\ \phi_{\mathrm{LDR}}(t) \\ \kappa_{\mathrm{LDR}}(t) \end{bmatrix} = \begin{bmatrix} X_{\mathrm{OLDR}}(t) \\ Y_{\mathrm{OLDR}}(t) \\ Z_{\mathrm{OLDR}}(t) \\ \omega_{\mathrm{OLDR}}(t) \\ \phi_{\mathrm{OLDR}}(t) \\ \kappa_{\mathrm{OLDR}}(t) \end{bmatrix} + \begin{bmatrix} a_X \\ a_Y \\ a_Z \\ a_\omega \\ a_\phi \\ a_\kappa \end{bmatrix} + (t - t_0) \begin{bmatrix} b_X \\ b_Y \\ b_z \\ b_\omega \\ b_\phi \\ b_\kappa \end{bmatrix} + (t - t_0)^2 \begin{bmatrix} c_X \\ c_Y \\ c_z \\ c_\omega \\ c_\phi \\ c_\kappa \end{bmatrix} \tag{6}$$

where t_0 is the reference time; $(X_{\mathrm{LDR}}(t), Y_{\mathrm{LDR}}(t), Z_{\mathrm{LDR}}(t), \omega_{\mathrm{LDR}}(t), \varphi_{\mathrm{LDR}}(t), \kappa_{\mathrm{LDR}}(t))$ are the true position and attitude angular values of laser scanner in the local reference frame at time t; $(X_{\mathrm{OLDR}}(t), Y_{\mathrm{OLDR}}(t), Z_{\mathrm{OLDR}}(t), \omega_{\mathrm{OLDR}}(t), \varphi_{\mathrm{OLDR}}(t), \kappa_{\mathrm{OLDR}}(t))$ are the position and attitude angular values of laser scanner in the local reference frame derived from POS observations at time t, lever arm bias, and coarse boresight angles; $(a_X, a_Y, a_Z, a_\omega, a_\varphi, a_\kappa, b_X, b_Y, b_Z, b_\omega, b_\varphi, b_\kappa, c_X, c_Y, c_Z, c_\omega, c_\varphi, c_\kappa)$ are the coefficients of correction polynomials for the laser scanner position and angular values, which will be abbreviated as position/angular correction coefficients hereinafter.

Substitute (6) into (2), then

$$\begin{bmatrix} X_P(t) \\ Y_P(t) \\ Z_P(t) \end{bmatrix} = \begin{bmatrix} X(a_X, b_X, c_X) \\ Y(a_Y, b_Y, c_Y) \\ Z(a_Z, b_Z, c_Z) \end{bmatrix} + R(a_\phi, a_\omega, a_\kappa, b_\phi, b_\omega, b_\kappa, c_\phi, c_\omega, c_\kappa) \begin{bmatrix} X_{\mathrm{PL}}(t) \\ Y_{\mathrm{PL}}(t) \\ Z_{\mathrm{PL}}(t) \end{bmatrix} \tag{7}$$

where $X(a_X, b_X, c_X)$, $Y(a_Y, b_Y, c_Y)$, and $Z(a_Z, b_Z, c_Z)$ are the true values of the laser scanner position in the local reference frame at time t, which are the functions of (a_X, b_X, c_X), (a_Y, b_Y, c_Y), and (a_Z, b_Z, c_Z), respectively. $R(a_\varphi, a_\omega, a_\kappa, b_\varphi, b_\omega, b_\kappa, c_\varphi, c_\omega, c_\kappa)$ is the rotation matrix of the true laser scanner attitude angles in the local reference frame at time t, which is the function of $(a_\varphi, a_\omega, a_\kappa, b_\varphi, b_\omega, b_\kappa, c_\varphi, c_\omega, c_\kappa)$.

For a certain LiDAR point P obtained at time t, its error-contaminated coordinates in the local reference frame can be found in the LiDAR strip file. The laser scanner position and attitude values in the local reference frame at time t can be calculated from sensor mounting parameters and POS position/attitude observations interpolated from the POS trajectory. Then, the point's coordinates $[X_{\mathrm{PL}}(t), Y_{\mathrm{PL}}(t), Z_{\mathrm{PL}}(t)]$ in the laser scanner frame can be calculated according to (2). If

its true ground coordinates in the local reference frame are known, this point can be used as a control point to calculate the position/angular correction coefficients. If the planimetric coordinates and the vertical coordinate are accurate, then this point can be viewed as a planimetric-vertical control point. If only the planimetric coordinate is accurate, it can be viewed as a planimetric control point. Taking the true coordinates of the control points $[X_P(t), Y_P(t), Z_P(t)]$ in the local reference frame as the observation value and their coordinates $[X_{\mathrm{PL}}(t), Y_{\mathrm{PL}}(t), Z_{\mathrm{PL}}(t)]$ in the laser scanner frame as the known numbers while the position/angular correction coefficients as unknowns, the error equation is therefore derived. As the angular related unknowns in $R(a_\varphi, a_\omega, a_\kappa, b_\varphi, b_\omega, b_\kappa, c_\varphi, c_\omega, c_\kappa)$ are inseparable, (7) is linearized, and the error equation is shown as follows:

$$V = Ar - L \tag{8}$$

where $V = [V_X, V_Y, V_Z]^T$ is the correction vector of the control points' coordinates in the local reference frame, $r = [\Delta a_X, \Delta a_Y, \Delta a_Z, \Delta a_\varphi, \Delta a_\omega, \Delta a_\kappa, \Delta b_X, \Delta b_Y, \Delta b_Z, \Delta b_\varphi, \Delta b_\omega, \Delta b_\kappa, \Delta c_X, \Delta c_Y, \Delta c_Z, \Delta c_\varphi, \Delta c_\omega, \Delta c_\kappa]^T$ are the correction vector of position/angular correction coefficients, A is the coefficient matrix of the unknowns, and L is the constant term of the error equation. The weight matrices of the planimetric-vertical control point and the planimetric control point are P_{HV} and P_H, respectively. Moreover

$$P_{\mathrm{HV}} = \begin{bmatrix} 1 & 0 & 0 \\ 0 & 1 & 0 \\ 0 & 0 & 1 \end{bmatrix} \quad P_H = \begin{bmatrix} 1 & 0 & 0 \\ 0 & 1 & 0 \\ 0 & 0 & 0 \end{bmatrix}. \tag{9}$$

All the control points can help build the error equations and find the solution to position/angular correction coefficients $(a_X, a_Y, a_Z, a_\varphi, a_\omega, a_\kappa, b_X, b_Y, b_Z, b_\varphi, b_\omega, b_\kappa, c_X, c_Y, c_Z, c_\varphi, c_\omega, c_\kappa)$ using the least squares method by iteration.

After getting the position/angular correction coefficients for each LiDAR strip, the coordinates of the LiDAR points in the local reference frame can be corrected. The procedures are as follows.

1) For each LiDAR point P, its error-contaminated coordinates $[X'_P(t), Y'_P(t), Z'_P(t)]^T$ in the local reference frame can be obtained from the LiDAR data file, and according to its acquisition time t, the POS position observations $[X_G(t), Y_G(t), Z_G(t)]T$ and the rotation matrix $R_I(t)$ in the local reference frame are calculated from the POS trajectory; thus, the laser scanner position/angular values $(X_{\mathrm{OLDR}}(t), Y_{\mathrm{OLDR}}(t), Z_{\mathrm{OLDR}}(t), \omega_{\mathrm{OLDR}}(t), \varphi_{\mathrm{OLDR}}(t), \kappa_{\mathrm{OLDR}}(t))$ can be obtained according to (3) and (4).
2) Combining with the coordinates $[X'_P(t), Y'_P(t), Z'_P(t)]^T$ and $(X_{\mathrm{OLDR}}(t), Y_{\mathrm{OLDR}}(t), Z_{\mathrm{OLDR}}(t), \omega_{\mathrm{OLDR}}(t), \varphi_{\mathrm{OLDR}}(t), \kappa_{\mathrm{OLDR}}(t))$, (2) is adopted to recover its coordinates $[X_{\mathrm{PL}}(t), Y_{\mathrm{PL}}(t), Z_{\mathrm{PL}}(t)]^T$ in the laser scanner frame at time t.
3) Based on the coefficients of correction polynomials $(a_X, a_Y, a_Z, a_\omega, a_\varphi, a_\kappa, b_X, b_Y, b_Z, b_\omega, b_\varphi, b_\kappa, c_X, c_Y, c_Z, c_\omega, c_\varphi, c_\kappa)$ computed in the LSA and the $(X_{\mathrm{OLDR}}(t), Y_{\mathrm{OLDR}}(t), Z_{\mathrm{OLDR}}(t), \omega_{\mathrm{OLDR}}(t), \varphi_{\mathrm{OLDR}}(t), \kappa_{\mathrm{OLDR}}(t))$, the corrected laser scanner position and attitude angle values $(X_{\mathrm{LDR}}(t), Y_{\mathrm{LDR}}(t), Z_{\mathrm{LDR}}(t), \omega_{\mathrm{LDR}}(t), \varphi_{\mathrm{LDR}}(t), \kappa_{\mathrm{LDR}}(t))$ can be obtained using (4). Integrated with the $[X_{\mathrm{PL}}(t), Y_{\mathrm{PL}}(t), Z_{\mathrm{PL}}(t)]^T$ acquired in step ②, the corrected coordinates $[X_P(t), Y_P(t), Z_P(t)]^T$ of the LiDAR point in the local reference frame can be recalculated using (2).

The above three procedures are iteratively conducted until all LiDAR points are rectified.

III. Multifeatures Matching Between Aerial Imagery and LiDAR Data

To conduct LSA, sufficient tie and control elements are required to build the error equations. Traditional LSA mainly considers the corresponding lines and plane features between overlapping point clouds as the tie elements. To extract sufficient corresponding information between adjacent strips, large strip overlap (50%) or cross-strips are required [8]–[10], [12], [15], [20]. On a flight mission aimed at producing orthophotos, the flight line is arranged according to the requirements for traditional aerophotogrammetry to save costs; thus, only a 30% overlap between the strips is guaranteed for the obtained digital aerial images. Laser scanning generally has a smaller field of view than that of aerial images. This smaller field results in a smaller overlap between the adjacent LiDAR strips, which is not advantageous to the conjugate features matching between strips. If the discrepancies between the LiDAR strip and the ground truth need to be improved, L-SGCTs should be installed. When the LiDAR strip errors are large due to the poor accuracy of the POS system, a large number of L-SGCTs are required, which is expensive and labor-intensive. On the contrary, some previous research proved that only a few P-SGCPs are needed to obtain satisfactory aerotriangulation accuracy for aerial images using POS-aided aerotriangulation [28], [29].

For these reasons, the aerotriangulated aerial images are used as reference data for the LSA in this paper. Aerotriangulation of the aerial images is performed using the current POS-aided aerotriangulation method in [28] and [29]. Then, two major types of conjugate features are matched between the triangulated aerial images and the LiDAR strips. The first type is the distinctive feature points matched between the aerial images and the LiDAR intensity images, and the second type is the corner features matched between the aerial images and the LiDAR point clouds.

A. Feature Points Matching Between Aerial Images and LiDAR Intensity Images

LiDAR intensity images are generated from the reflectance signals of the laser foot points recorded in the LiDAR data files. In this paper, the triangulated irregular network (TIN) of the LiDAR points is built, then the LiDAR intensity images are obtained through regularly interpolating the TIN (the interpolating distance is about 1/3 of the point distance). The conjugate points between the LiDAR intensity images and the triangulated aerial

images are matched to obtain the control points for LSA. The specific procedures are as follows.

Step 1) Based on the coordinates and intensity information of the LiDAR point clouds, the LiDAR intensity images and digital surface models (DSMs; similar to LiDAR intensity image, the DSM is obtained by regularizing the LiDAR points to image, and the pixel value of the image denotes the elevation) are obtained through interpolating the TIN of the LiDAR points.

Step 2) The aerial images are downsampled to have the ground sampling distance the same as 1/3 times the average LiDAR point space, and the Harris feature points are extracted on the downsampled aerial images.

Step 3) For each Harris feature point extracted on the downsampled aerial images, a matching window, which centers on this point with a size of $n \times n$ pixels (n is the size of the matching window, which can always be set as a value from 15 to 19, e.g., 17 in this paper) on the downsampled aerial image, is defined. Assuming that the image coordinates of this feature point and its four corners are $(i_{\mathrm{Am}}, j_{\mathrm{Am}})$ $(m = 1, \ldots, 5;\ A$ represents aerial image), using the photogrammetric collinearity equation to project the feature point and four corners onto the DSM, the corresponding coordinates in the local reference frame $(X_{\mathrm{Dm}}, Y_{\mathrm{Dm}}, Z_{\mathrm{Dm}})$ $(m = 1, \ldots, 5;\ D$ represents DSM) are obtained, and thus, the image coordinates on LiDAR intensity image $(i_{\mathrm{Ik}}, j_{\mathrm{Ik}})$ $(k = 1, \ldots, 5;\ I$ represents LiDAR intensity image). Then, the affine transformation model is adopted to calculate the local transformation relationship between the downsampled image and the LiDAR intensity image, and then, the searching window is interpolated from the intensity image. The rotation angle and scale discrepancy between the downsampled aerial images and the LiDAR intensity images can be eliminated using the affine transformation. Grey correlation coefficient matching is conducted between the matching window and the searching window to acquire the conjugate point.

Step 4) If the feature point extracted on the downsampled aerial image is successfully matched to a conjugate point on the LiDAR intensity image, its conjugate points are then matched between the current downsampled aerial image and its overlapping downsampled aerial images. Then, the ground coordinates (X_{A1}, Y_{A1}, Z_{A1}) of the feature point in the local reference frame are calculated using the space intersection and using the coordinates as the true value (reference coordinates). The coordinate pair (X_{A1}, Y_{A1}, Z_{A1}) and (X_{D1}, Y_{D1}, Z_{D1}) is used as the control point in LSA. The principal to judge the attribute of the control point is to draw a circle around the point with a certain radius (about 2.5 times the average LiDAR point distance) in the LiDAR strip, obtain the elevation of the points that fall in the circle, and calculate the difference between the maximum and the minimum. If the difference is less than the threshold [the threshold can be set as a value slightly smaller than the expected elevation accuracy of LiDAR points after LSA (i.e., the elevation accuracy of aerotriangulation), and in this paper, the threshold is set as 0.1 m], the control point is located on a flat area and can be viewed as a planimetric-vertical control point. Otherwise, the interpolated elevation of the feature point might consist of large errors and, therefore, is merely qualified as a planimetric control point.

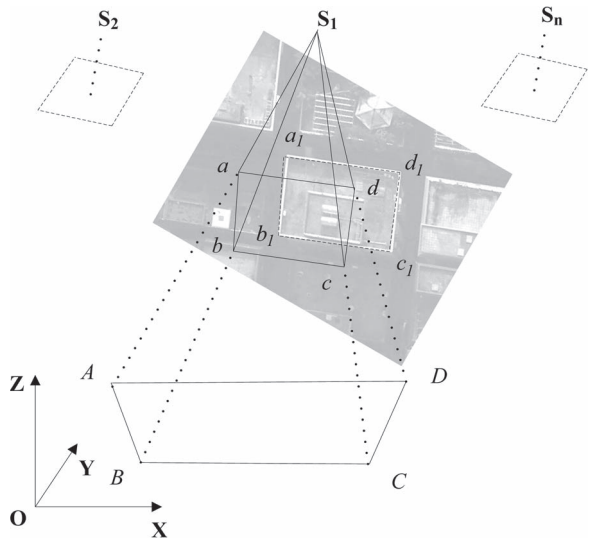

Fig. 1. Demonstration of conjugate BCF matching between LiDAR data and aerial images (where the quadrangle ABCD indicates the building contour in LiDAR data, the dotted quadrangles represent the overlapping aerial images, $S1, S2, \ldots, Sn$ (n is the index of overlapping images, $n \geq 2$) represents the photographing center of the aerial images, the quadrangle $abcd$ represents the back-projected contour lines of the LiDAR building contour $ABCD$, and the quadrangle $a_1b_1c_1d_1$ represents the building contour lines extracted from the aerial images).

B. Building Corner Features Matching Between Aerial Images and LiDAR Data

In our previous work [35], a building contour extraction algorithm based on the TIN of point clouds is proposed and used to obtain building corner features (BCFs) from discrete point clouds. In this paper, building straight-line contours and BCFs are extracted using the method in [35], and conjugate BCFs are matched between the aerial images and the LiDAR data. The BCF is constituted by two adjacent building straight-line edges. The BCF extracted from the LiDAR data is named the LiDAR BCF. Details about the LiDAR BCF extraction method based on TIN can be found in [35].

In this paper, the conjugate BCFs matched between the LiDAR strip and the aerial images are referred to as control information in LSA. Fig. 1 shows the conjugate BCFs matching between the LiDAR data and the aerial images. First, edge detection is conducted through the Canny algorithm and straight-line fitting on aerial images to obtain image building straight-line edges. Second, for each LiDAR BCF,

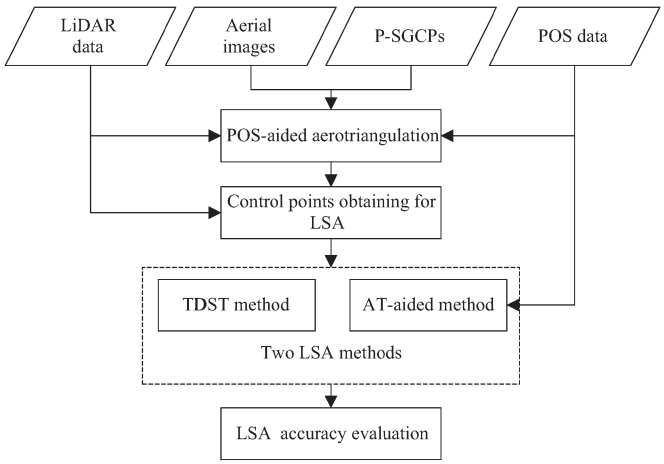

Fig. 2. Workflow of LSA in this paper.

the photogrammetric collinearity equation is used to back-project the two line segments of the LiDAR BCF onto the corresponding aerial images; as shown in Fig. 1, the back-projected BCF (abc in Fig. 1) is obtained through back-projecting the LiDAR BCF ABC (in Fig. 1) onto aerial image S_1. Each building straight-line edge near the back-projected BCF is checked and combined with its adjacent and nearly orthogonal edges to be the aerial image BCF (such as $a_1b_1c_1$ in Fig. 1). Through comparing the length, intersection angle, and center point distance of the lines of the back-projected BCF with that of the aerial image BCF, whether they are conjugate BCFs can be judged. Finally, matching the conjugate aerial image BCFs of the LiDAR BCF ABC continues on the rest of the overlapping aerial images ($S_2, \ldots, S_n$; n is the index of the overlapping images, $n \geq 2$), and the conjugate aerial image BCFs are assumed to be $(a_2b_2c_2, \ldots, a_nb_nc_n)$. For midpoint $B(X, Y, Z)$ on the LiDAR BCF ABC, $(b_1, b_2, \ldots, b_n)$ are its conjugate points on each overlapping aerial image. Knowing the accurate exterior orientation parameters of the aerial images, the space intersection can be adopted to calculate the ground coordinates $B_I(X_I, Y_I, Z_I)$ of the image points $(b_1, b_2, \ldots, b_n)$ on the local reference frame. In this case, coordinates pair $B_I(X_I, Y_I, Z_I)$ and $B(X, Y, Z)$ can be viewed as a planimetric-vertical control point on LSA.

IV. Workflow of LSA

The workflow of LSA in this paper is shown in Fig. 2. First, aerotriangulation of the aerial image is conducted with the assistance of the LiDAR data, the POS data, and a few P-SGCPs. Second, the two methods introduced in Section III are adopted to automatically match the conjugate points and the conjugate BCFs between the aerial images and the LiDAR data, from which the planimetric control points and planimetric-vertical control points are obtained. These control points are used further to conduct LSA using the proposed AT-aided LSA method. To do comparison with the proposed AT-aided LSA method, the TDST LSA method is also used to conduct LSA. The TDST is similar to the rigid body transformation used in [8], [9], [11], [14], and [15], but an extra scale factor is resolved in TDST. Seven transformation parameters

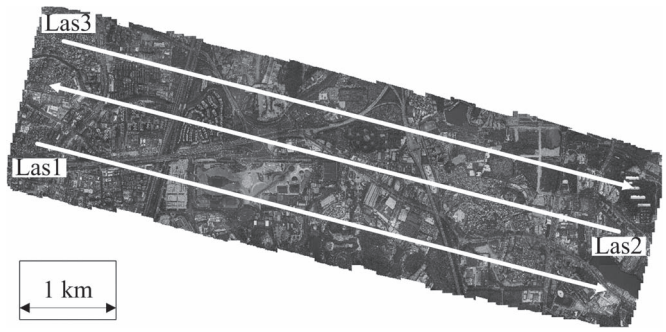

Fig. 3. Orthophoto of the test field and the distribution of three LiDAR strips.

are calculated in TDST for each LiDAR strip, namely, the scale coefficient λ, the three rotation angles (Φ, ω, κ), and the three translation quantities $(\Delta X, \Delta Y, \Delta Z)$. Finally, the accuracy of the LiDAR strips after the LSA is assessed, including the vertical discrepancy analysis between the LiDAR strips, the absolute planimetric accuracy, and the absolute vertical accuracy of the LiDAR strips.

Considering that, when obtaining control points, many LSA control points are derived from image matching between LiDAR intensity image and downsampled aerial image, the coordinate accuracy (particularly the vertical coordinate accuracy) of LSA control points may be reduced. To achieve high vertical accuracy in the LSA, a group of vertical control points is used in the LSA. First, dense conjugate points matching (about 5000 image points per image) are performed using the raw aerial images, and dense ground points are intersected using accurate image exterior orientation parameters. To guarantee the coordinate accuracy of the intersected ground points, only the k-ray points ($\mathrm{k} > 2$, i.e., each matched image point has at least two conjugate image points on the other images) are used. Second, for each ground point, its adjacent LiDAR points located in a circle (the radius of the circle is set to be five times the average LiDAR point space, e.g., 2.5 m in this paper) centered at this point are searched out in corresponding LiDAR strip. If the differential of maximum and minimum vertical coordinates of the adjacent points is smaller than a threshold (which can be set slightly smaller than the expected elevation accuracy of LiDAR points after LSA, e.g., 0.10 m in this paper), the point locates in local flat area and can be treated as vertical control point in LSA. The conjugate point in corresponding LiDAR strip for this control point is selected as the nearest LiDAR point in this LiDAR strip. The weight matrices of the vertical control point is

$$P_V = \begin{bmatrix} 0 & 0 & 0 \\ 0 & 0 & 0 \\ 0 & 0 & 1 \end{bmatrix}. \tag{10}$$

As mismatching is inevitable, there may be blunders in the obtained LSA control points. To eliminate the blunders, iterative least squares weighted solution [36] is adopted in the LSA procedure. After each iteration step of LSA, the weight of each LSA control point will be recalculated according to its residuals in the previous LSA step. Control points with small residuals will get larger weights than that with big residuals, and the blunders will gradually be removed during the iteration.

TABLE I
COORDINATE RESIDUALS OF CONTROL POINTS AND CHECK POINTS AFTER AEROTRIANGULATION (UNITS: m)

Point Types	RMSE of Residuals		Mean of Residuals		Maximum of Residuals	
	Planimetric	Vertical	Planimetric	Vertical	Planimetric	Vertical
Control Point	0.09	0.08	0.08	0.0009	0.17	0.15
Check Point	0.12	0.06	0.11	0.02	0.24	0.15

V. EXPERIMENTS AND ANALYSIS

A. Experimental Data

To verify the feasibility of the proposed AT-aided LSA method and the multifeature matching method, three strips of airborne LiDAR point clouds (named $Las1$, $Las2$, and $Las3$, respectively) and simultaneously obtained digital aerial images were used to do the experiment. The data were acquired in 09/2011 in Guangzhou, China. The LiDAR data were obtained with a Trimble Harrier 68i LiDAR system equipped with POS AV 510 at a mean relative flight height of 700 m with a mean point density of approximately 4.8 points/m^2 and an average point distance of about 0.50 m. The laser foot point size was about 0.35 m. The optical sensor mounted together with LiDAR system was Rollei Metric AIC Pro (format size: 8984 pixels $\times$ 6732 pixels; pixel size: 0.006 mm; focal length: 51.695 mm). The ground sampling distance of the aerial images is about 0.09 m. The frame rate of the camera is about 5.5 s. Each strip consists of 28 images; hence, the flight time of each strip is about 2.6 min. The orthophoto of the test field and the distribution of the three LiDAR strips are shown in Fig. 3. The overlap of adjacent LiDAR strips is about 28%. The forward overlap and side overlap of the aerial images are approximately 60% and 30%, respectively. In the manufacture's specifications, the position accuracy of POS AV 510 is 0.05–0.3 m, and the orientation angular accuracy is 0.005° for pitch and roll and 0.008° for heading. The lever arm bias are -0.077, -0.045, and 0.177 m for x, y, and z, respectively, which are treated as without errors. The coarse estimations of mounting angles are all set as zero for heading, roll, and pitch. Generally speaking, the accuracy of POS AV 510 will be high if adequate reference GPS stations are well installed, and GPS/IMU data postprocessing is correctly done. However, in our case, only one reference GPS station was available and even that one was far away from the survey area; hence, the accuracy of the POS data we obtained was low, and the acquired LiDAR data suffered obvious POS systematic errors (particularly the vertical shift errors).

B. Results of Aerotriangulation

Twenty-eight P-SGCPs were surveyed using GPS RTK on the test field, and their coordinate accuracy was about 0.05 m. Seven of them were selected as control points, which were evenly located on the corners and the center of the test field, and the remaining 21 points were used as check points in aerotriangulation. As shown in Table I, after POS-aided aerotriangulation, the maximum of the planimetric and vertical coordinate residuals of the control points were 0.17 and 0.15 m, respectively, and the maximum of the planimetric and vertical coordinate residuals of the check points were 0.24 and 0.15 m, respectively. The results show that the aerotriangulation achieved good accuracy, which can meet the requirements of aerotriangulation for topographic mapping at 1:1000 scale for flat terrain [37] in China, as shown in Table II.

TABLE II
ACCURACY REQUIREMENTS OF AEROTRIANGULATION FOR TOPOGRAPHIC MAPPING AT 1:1000 SCALE IN CHINA (UNITS: m)

Terrain Types	*Maximum Allowed Error*			
	Control Point		Check Point	
	Planimetric	Vertical	Planimetric	Vertical
Flat Terrain	0.30	0.20	0.50	0.28

C. Conjugate Multifeatures Matching Results

1) Results of Distinctive Points Matching Between Aerial Images and LiDAR Intensity Images: A total of 16 164 pairs of conjugate points were matched between the downsampled aerial images and the LiDAR intensity images. Among them, 4247 pairs were on $Las1$, including 1771 pairs of planimetric-vertical control points and 2476 pairs of planimetric control points; 5962 pairs were on $Las2$, including 2106 pairs of planimetric-vertical control points and 3856 pairs of planimetric control points; and 5955 pairs were on $Las3$, including 2141 pairs of planimetric-vertical control points and 3814 pairs of planimetric control points. A portion of the matching results is shown in Fig. 4. There are certain scale and angular discrepancies between the LiDAR intensity images and the downsampled aerial images. However, as shown in Fig. 4, adopting the proposed conjugate points matching method can match conjugate points like pavement marking feature points and building roof corner points well.

2) Results of Conjugate BCFs Matching Between Aerial Images and LiDAR Point Clouds: Using the proposed conjugate BCF matching method, a total of 1200 pairs of conjugate points were matched between the aerial images and the LiDAR data. Among them, 357 pairs were on $Las1$, 565 pairs were on $Las2$, and 278 pairs were on $Las3$. An example of BCF matching result is shown in Fig. 5.

3) Results of Vertical Control Points Obtaining for LSA: A total of 72 561 ground points were matched and intersected from the raw aerial images. Then, 8523 vertical LSA control

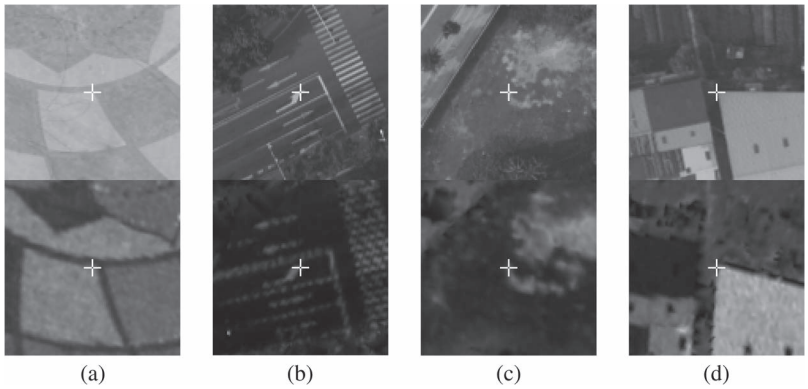

Fig. 4. Part of the conjugate points matched between the downsampled aerial images and the LiDAR intensity images. There are four sets of matching results (a), (b), (c), and (d). The upper half of each set is the downsampled aerial image feature point, and the bottom half is the conjugate point matched on the LiDAR intensity image (the cross indicates their locations).

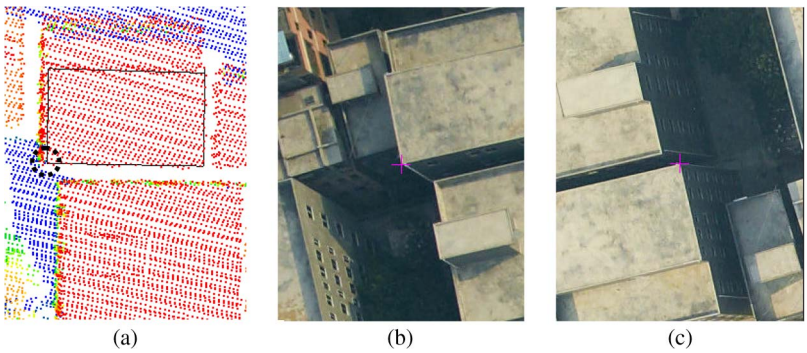

Fig. 5. Result of conjugate BCFs matching. The picture in (a) is the LiDAR points, and the black lines denote the extracted building edges. The building corner matched with aerial images is denoted in (a) by a black circle; the pictures in (b) and (c) denote the matched corner points on two aerial images with crosses. The two images are from very different perspectives.

points were obtained in $Las1$; 10 960 vertical LSA control points were obtained in $Las2$; and 4851 vertical LSA control points were obtained in $Las3$.

It is important to mention that as the accurate aerial image exterior orientation parameters were obtained during the aerotriangulation, all the conjugate images matched in the above a, b, c procedures in this section are first checked using space intersection, and only the image points that have residuals smaller than 1 pixel are considered to be used as LSA control points.

D. Results of LSA

1) Analysis of the LiDAR Strip Planimetric Coordinate Accuracy Before and After LSA: To analyze the planimetric coordinate accuracy of each LiDAR strip, 37 pairs of manually measured conjugate points between the aerial images and the LiDAR intensity images were used as planimetric check points. They were mainly the obvious feature points like zebra strips' endpoints and roof corner points. There were 10, 14, and 13 planimetric check points on $Las1$, $Las2$, and $Las3$, respectively. According to their point coordinates on the aerial images, the coordinates in the local reference frame of the planimetric check points were calculated through the space intersection using the image exterior orientation parameters obtained in aerotriangulation. Since the accuracy of aerotriangulation was very good, as shown in Table I, the intersected coordinates in the local frame could be regarded as the ground truth and used as a reference. Then, the planimetric coordinates of the check points in the LiDAR strip were calculated using its image coordinates measured in the LiDAR intensity images. The differences between the reference planimetric coordinates and the planimetric coordinates in the LiDAR strip, also known as the check point planimetric residuals, were computed. Fig. 6 shows the planimetric coordinate residuals dXY ($dXY = \sqrt{dX * dX + dY * dY}$, dX and dY represent the X

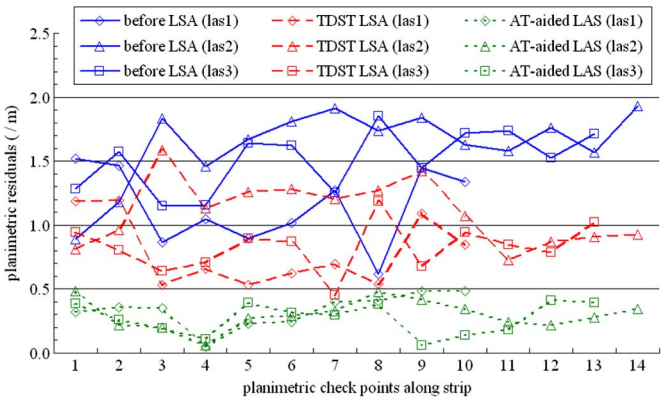

Fig. 6. Planimetric coordinate residuals of the planimetric check points before and after LSA on $LAS1$, $LAS2$, $LAS3$, respectively.

TABLE III
PLANIMETRIC COORDINATE RESIDUALS OF CHECK POINTS BEFORE AND AFTER LSA (UNITS: m)

Planimetric		*Before LSA*			*TDST method*			AT-aided method		
residuals		Las1	Las2	Las3	Las1	Las2	Las3	Las1	Las2	Las3
dX	MEAN	0.91	-1.56	1.44	0.62	-0.99	0.71	0.14	-0.13	0.16
	RMSE	0.96	1.58	1.45	0.68	1.03	0.73	0.28	0.20	0.22
	MAX	1.31	-1.93	1.72	1.07	-1.51	1.01	0.39	-0.38	0.39
dY	MEAN	-0.62	0.33	-0.05	-0.35	0.29	0.09	0.10	0.03	0.12
	RMSE	0.70	0.47	0.43	0.47	0.45	0.43	0.22	0.25	0.20
	MAX	-1.03	1.05	-0.92	-0.68	0.86	-0.84	-0.33	-0.47	0.41
dXY	MEAN	1.15	1.63	1.51	0.79	1.10	0.83	0.33	0.30	0.27
	RMSE	1.18	1.65	1.53	0.83	1.13	0.85	0.36	0.32	0.30
	MAX	1.52	1.93	1.85	1.19	1.58	1.19	0.49	0.48	0.41

coordinate residual and the Y coordinate residual, respectively) of the planimetric check points on $Las1$, $Las2$, and $Las3$ before and after LSA. As can be seen from the figure, obvious planimetric errors exist on all three strips before LSA. After adopting TDST LSA, the planimetric errors are just slightly reduced. However, after using the AT-aided LSA method, the planimetric errors on all three strips show significant improvement.

Table III lists the statistics of the planimetric coordinate residuals dXY of the planimetric check points before and after LSA. As shown in Table III, the root mean square error (RMSE) of the planimetric coordinate residuals of the planimetric check points on the three LiDAR strips before LSA are 1.18, 1.65, and 1.53 m, respectively. The LiDAR strips all have a large number of planimetric coordinate errors. After using the TDST LSA method, the three RMSEs are reduced to 0.83, 1.13, and 0.85 m, respectively. The three LiDAR strips still have large magnitude of errors. After adopting the proposed AT-aided LSA method, the three RMSEs are reduced to 0.36, 0.32, and 0.30 m, respectively. Considering that the average point distance of the LiDAR point cloud is around 0.5 m and the planimetric coordinate accuracy of the check points measured on the LiDAR intensity images are approximately one pixel (0.2 m), the planimetric coordinate error correction effects of the three strips are generally ideal. The coordinate accuracy after AT-aided LSA is about 0.6 times the average LiDAR point distance.

From the experimental results shown in Fig. 6 and Table III, the AT-aided LSA method can significantly improve the planimetric coordinate accuracy on LiDAR strips with large planimetric errors. The planimetric coordinate residuals after AT-aided LSA can reach 0.6 times the average LiDAR point distance. The results of the proposed AT-aided LSA method are obviously superior to that of the TDST method.

2) Vertical Accuracy Analysis:

a) Vertical discrepancies between overlapping LiDAR strips: To evaluate the vertical discrepancies between the overlapping LiDAR strips, several positions in the overlapping area of each pair of overlapping LiDAR strips were selected to compute the vertical coordinate differences between the two strips. Specifically, point locations were selected at an interval of 3 m along the flight direction in the overlapping area, and the elevation values of all the LiDAR points were searched within a certain radius around the point (the radius can be set as about 2.5 times the average LiDAR point distance) in any one LiDAR strip. If the difference between the maximum and the minimum elevation was less than the threshold (which can be set slightly smaller than the expected elevation accuracy of LiDAR points after LSA, e.g., 0.10 m in this paper), the point was assumed to be located on a flat area and can be viewed as a vertical check point. For each vertical check point, its elevation can be calculated through interpolation on both of the overlapped LiDAR strips. The discrepancies of the elevation value between the two strips of the vertical check points can be used to evaluate the vertical discrepancies between the LiDAR strips.

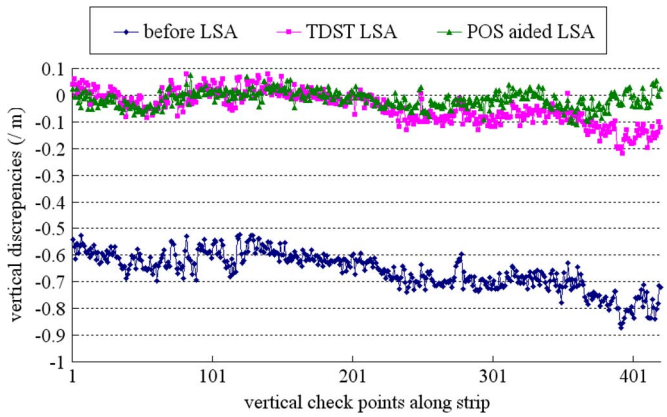

Fig. 7. Vertical discrepancies between $Las1$ and $Las2$ before and after LSA.

Fig. 7 shows the discrepancies between $Las1$ and $Las2$ before and after LSA. Fig. 8 shows the discrepancies between $Las2$ and $Las3$ before and after LSA. The horizontal axis represents the index of vertical check points selected along

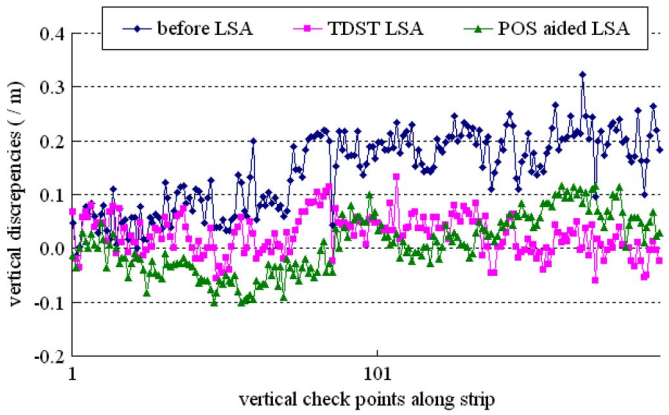

Fig. 8. Vertical discrepancies between $Las2$ and $Las3$ before and after LSA.

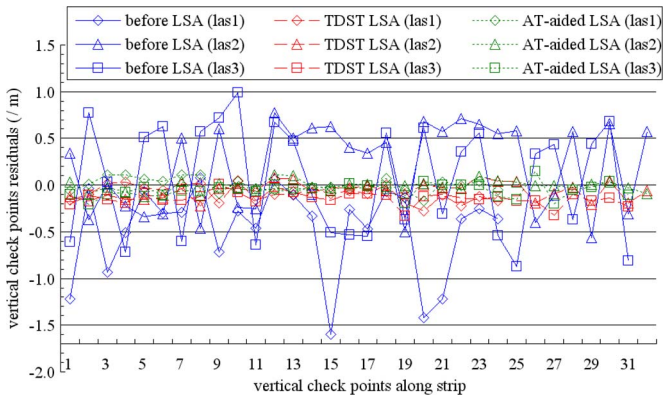

Fig. 9. Vertical coordinate residuals of the vertical check points before and after LSA on $LAS1$, $LAS2$, $LAS3$, respectively.

the flight direction on the LiDAR strips. The vertical axis represents the vertical discrepancies of the vertical check points between the overlapping strips. As shown in Fig. 7, the vertical discrepancies of the vertical check points on $Las1$ and $Las2$ along the flight direction fluctuate between -0.90 and -0.50 m. The vertical discrepancies are obviously reduced both after TDST LAS and AT-aided LSA, but the discrepancies after using AT-aided LSA are slightly smaller than those after using TDST LSA. After AT-aided LSA, the vertical discrepancies are obviously reduced to a magnitude between -0.10 and 0.10 m.

In Fig. 8, before LSA, the vertical discrepancies of the vertical check points on $Las2$ and $Las3$ fluctuate between -0.02 and 0.32 m. The vertical discrepancies are obviously reduced both after TDST LAS and AT-aided LSA, and most of the discrepancies fluctuate between -0.10 and 0.10 m.The TDST LAS and the AT-aided LAS seem to have the same good effect on reducing the discrepancies between $Las2$ and $Las3$.

As can be seen from the experimental results shown in Fig. 7 and Fig. 8, adopting the proposed AT-aided LSA method can well improve the vertical discrepancies between the LiDAR strips. Moreover, the proposed AT-aided LSA method is slightly superior to the TDST LSA method in reducing the vertical discrepancies between adjacent LiDAR strips (the two methods are similar in Fig. 8, but the AT-aided LSA method is better in Fig. 7).

2) Analysis of the absolute vertical accuracy of the LiDAR strips: To further analyze the absolute vertical accuracy of each LiDAR strip, 72 image tie points located in a flat region were precisely measured on the aerial images, and their coordinates were calculated in the local reference frame by the space intersection using the image exterior orientation parameters obtained in aerotriangulation. The intersected coordinates of these points were viewed as the ground truth concerning the high accuracy of aerotriangulation. Then, along with the above 28 P-SGCPs, they were used to determine if they were located in a flat region so they can be used as the vertical check points of the LiDAR strips. There were 24 vertical check points in $Las1$, 32 vertical check points in $Las2$, and 31 vertical check points in $Las3$. The LiDAR strip's vertical accuracy can be measured by calculating the discrepancies (also called the vertical coordinate residuals of the vertical check points) between the ground truth coordinates of the check points and their interpolated vertical coordinates in the LiDAR strip. Fig. 9 presents the vertical coordinate residuals of the vertical check points on $Las1$, $Las2$, and $Las3$, respectively, before and after LSA. The vertical coordinate errors of the three LiDAR strips are obvious before the LSA. After TDST LSA, the improvement is obvious but still not ideal. When the AT-aided LSA method is introduced, all three strips show significant improvement on the vertical coordinate residuals.

The statistics of the mean, the RMSE, and the maximum of the vertical coordinate residuals of the vertical check points on the three LiDAR strips before and after LSA are shown in Table IV. According to the corrected results of the three LiDAR strips, the vertical precision of the point clouds after adopting the AT-aided LSA method is 0.1 m. The largest vertical residual is smaller than 0.2 m, which shares the same level of vertical accuracy with aerotriangulation as shown in Table I. Obviously, the AT-aided LSA is better than the TDST LSA.

VI. Conclusion and Recommendations for Future Research

For the purpose of researching LSA for LiDAR strips acquired by low-precision LiDAR systems used in China, this paper has presented a rigorous LSA method that adopts aerial images of the same area as the control information. Owing to the fact that POS shift/drift errors always exist for the low-precision POS system, POS shift/drift errors and boresight angular errors are the major concern in the LSA procedure in this paper. This paper first introduced the AT-aided LSA mathematic models. The adjustment models were derived from the LiDAR geolocation equation and, thus, were rigorous. Then, this paper proposed a method for obtaining the control elements needed in LSA. Aerotriangulated aerial images located in the same area with the LiDAR data were used in this method as the reference data for LSA. Conjugate points and conjugate BCFs were matched between LiDAR strips and aerial images with the proposed two matching methods, respectively.

The feasibility of the developed AT-aided LSA method and the multifeature matching method were tested using a real data set, and comparison experiments also were performed using the TDST LSA method. Both the discrepancies between the adjacent LiDAR strips and the discrepancies between the

TABLE IV
VERTICAL COORDINATE RESIDUALS OF VERTICAL CHECK POINTS BEFORE AND AFTER LSA (UNITS: m)

Strip No.	mean			RMSE			*maximum*		
	Before LSA	TDST method	POS aided method	Before LSA	TDST method	POS aided method	Before LSA	TDST method	POS aided method
1	-0.47	-0.09	0.001	0.66	0.12	0.07	-1.60	-0.28	-0.17
2	0.21	-0.06	-0.01	0.49	0.10	0.06	0.77	-0.22	-0.12
3	0.06	-0.14	-0.05	0.58	0.16	0.09	0.99	-0.33	-0.20

LiDAR strips and the ground truth were examined before and after LSA. The experimental results of all three LiDAR strips revealed that the proposed AT-aided LSA method achieved high planimetric rectification precision and high vertical rectification precision. The results also demonstrated that the proposed AT-aided LSA method is far superior to the TDST LSA method.

This paper uses P-SGCPs to achieve alignment between the LiDAR strips and the ground truth. Compared with methods using L-SGCTs, the method in this paper is superior for the following reasons. First, unlike L-SGCTs, P-SGCPs do not need to be specially manufactured because natural objects on the ground usually can serve P-SGCPs. Second, P-SGCPs can be determined and measured after the mission at any time, and the optimal locations for the P-SGCPs can be chosen by analyzing the overlap between the aerial images. On the other hand, L-SGCTs must be installed before the flight mission, and they are sometimes missed in the LiDAR strips owing to the overlap fluctuation of LiDAR strips.

As a large amount of control points come from the matching results between the LiDAR intensity images and aerial images, the LiDAR data should have good intensity information. This paper used simultaneously obtained aerial images and LiDAR points as experimental data set, but LiDAR data and aerial images obtained at different times can also be used as long as the two types of data sets are on the same area and the land cover change is trivial. The ground sampling distance of aerial images is recommended to be smaller than 1/3 times the average LiDAR point distance, with the purpose of providing accurate control points for LSA.

Since the digital camera and LiDAR system are usually mounted together on the aircraft, their position and attitude are measured by the same POS. That is to say, the position and attitude values of both the digital camera and the LiDAR system encounter the same POS shift/drift errors. Therefore, the combined block adjustment of LiDAR strips and aerial images is theoretically feasible and will be addressed in future work.

ACKNOWLEDGMENT

The authors would like to thank the anonymous reviewers and members of the editorial team for the comments and contributions and M. Wang from the University of South Florida, Tampa, FL, USA, for refining the use of English in this paper.

REFERENCES

[1] J. Shan and C. K. Toth, *Topographic Laser Ranging and Scanning: Principles and Processing*. Boca Raton, FL, USA: CRC Press, 2008, pp. 445–477.
[2] D. Gonzalez-Aguilera, E. Crespo-Matellan, D. Hernandez-Lopez, and P. Rodriguez-Gonzalvez, "Automated urban analysis based on LiDAR-derived building models," *IEEE Trans. Geosci. Remote Sens.*, vol. 51, no. 3, pp. 1844–1851, Mar. 2013.
[3] X. Liu, Z. Zhang, J. Peterson, and S. Chandra, "LiDAR-derived high quality ground control information and DEM for image orthorectification," *GeoInformatica*, vol. 11, no. 1, pp. 37–53, Mar. 2007.
[4] W. Yao, S. Hinz, and U. Stilla, "Extraction and motion estimation of vehicles in single-pass airborne LiDAR data towards urban traffic analysis," *ISPRS J. Photogramm. Remote Sens.*, vol. 66, no. 3, pp. 607–611, May 2011.
[5] E. P. Baltsavias, "Airborne laser scanning: Basic relations and formulas," *ISPRS J. Photogramm. Remote Sens.*, vol. 54, no. 2/3, pp. 199–214, Jul. 1999.
[6] A. Wehr and U. Lohr, "Airborne laser scanning—An introduction and overview," *ISPRS J. Photogramm. Remote Sens.*, vol. 54, no. 2/3, pp. 68–82, Jul. 1999.
[7] S. Filin, "Recovery of systematic biases in laser altimetry data using natural surfaces," *Photogramm. Eng. Remote Sens.*, vol. 69, no. 11, pp. 1235–1242, Nov. 2003.
[8] A. F. Habib, A. P. Kersting, K.-I. Bang, R. Zhai, and M. Al-Durgham, "A strip adjustment procedure to mitigate the impact of inaccurate mounting parameters in parallel LiDAR strips," *Photogramm. Rec.*, vol. 24, no. 126, pp. 171–195, Jun. 2009.
[9] A. Habib, A. P. Kersting, K. I. Bang, and D. C. Lee, "Alternative methodologies for the internal quality control of parallel LiDAR strips," *IEEE Trans. Geosci. Remote Sens.*, vol. 48, no. 1, pp. 221–236, Jan. 2010.
[10] P. Kumari, W. E. Carter, and R. L. Shrestha, "Adjustment of systematic errors in ALS data through surface matching," *Adv. Space Res.*, vol. 47, no. 10, pp. 1851–1864, May 2011.
[11] J. Lee, K. Yu, Y. Kim, and A. F. Habib, "Adjustment of discrepancies between LIDAR data strips using linear features," *IEEE Geosci. Remote Sens. Lett.*, vol. 4, no. 3, pp. 475–479, Jul. 2007.
[12] J. Willers *et al.*, "A post-processing step error correction algorithm for overlapping LiDAR strips from agricultural landscapes," *Comput. Electron. Agric.*, vol. 64, no. 2, pp. 183–193, Dec. 2008.
[13] M. J. E. Crombaghs, R. Brügelmann, and E. J. Min, "On the adjustment of overlapping strips of laser altimeter height data," in *Proc. Int. Arch. Photogramm. Remote Sens.*, 2000, vol. 33, no. B3/1, pp. 224–231.
[14] G. Vosselman, "Analysis of planimetric accuracy of airborne laser scanning surveys," in *Proc. Int. Arch. Photogramm., Remote Sens. Spatial Inf. Sci.*, 2008, vol. 37, no. B3a, pp. 99–104.
[15] M. Rentsch and P. Krzystek, "Lidar strip adjustment with automatically reconstructed roof shapes," *Photogramm. Rec.*, vol. 27, no. 139, pp. 272–292, Sep. 2012.
[16] H. G. Maas, "Methods for measuring height and planimetry discrepancies in airborne laser scanner data," *Photogramm. Eng. Remote Sens.*, vol. 68, no. 9, pp. 933–940, Sep. 2002.
[17] C. K. Toth, "Calibrating Airborne LIDAR Systems," in *Proc. ISPRS Commiss. II Symp.*, Xi'an, China, Aug. 20–23, 2002, pp. 475–480.
[18] J. Skaloud and D. Lichti, "Rigorous approach to bore-sight self-calibration in airborne laser scanning," *ISPRS J. Photogramm. Remote Sens.*, vol. 61, no. 1, pp. 47–59, Oct. 2006.

[19] M. Favalli, A. Fornaciai, and M. T. Pareschi, "LIDAR strip adjustment: Application to volcanic areas," *Geomorphology*, vol. 111, no. 3/4, pp. 123–135, Oct. 2009.
[20] M. Hebel and U. Stilla, "Simultaneous calibration of ALS systems and alignment of multiview LiDAR scans of urban areas," *IEEE Trans. Geosci. Remote Sens.*, vol. 50, no. 6, pp. 2364–2379, Jun. 2012.
[21] A. Habib, K. I. Bang, A. P. Kersting, and D.-C. Lee, "Error budget of LiDAR systems and quality control of the derived data," *Photogramm. Eng. Remote Sens.*, vol. 75, no. 9, pp. 1093–1108, Sep. 2009.
[22] S. Filin and G. Vosselman, "Adjustment of airborne laser altimetry strips," in *Proc. Int. Arch. Photogramm., Remote Sens. Spatial Inf. Sci.*, 2004, vol. 35, no. B3, pp. 285–289.
[23] H. Burman, "Adjustment of laser scanner data for correction of orientation errors," in *Proc. Int. Arch. Photogramm., Remote Sens. Spatial Inf. Sci.*, 2000, vol. 33, no. B3/1, pp. 125–132.
[24] N. Pfeifer, S. O. Elberink, and S. Filin, "Automatic tie elements detection for laser scanner strip adjustment," in *Proc. Int. Arch. Photogramm., Remote Sens. Spatial Inf. Sci.*, Sep. 2005, vol. 36, no. 3/W19, pp. 174–179.
[25] G. Vosselman, "On the estimation of planimetric offsets in laser altimetry data," in *Proc. IAPSIS*, 2002, vol. 34, no. 3A, pp. 375–380.
[26] P. Friess, "Toward a rigorous methodology for airborne laser mapping," in *Proc. EuroCOW*, Castelldefels, Spain, Jan. 25–27, 2006, pp. 25–27.
[27] N. Csanyi and C. K. Toth, "Improvement of LiDAR data accuracy using LiDAR-specific ground targets," *Photogramm. Eng. Remote Sens.*, vol. 73, no. 4, pp. 385–396, Apr. 2007.
[28] Y. Zhang, X. Xiong, X. Shen, and Z. Ji, "Bundle block adjustment of weakly connected aerial imagery," *Photogramm. Eng. Remote Sens.*, vol. 78, no. 9, pp. 983–989, Sep. 2012.
[29] X. Yuan, "A novel method of systematic error compensation for a position and orientation system," *Progress Natural Sci.*, vol. 18, no. 8, pp. 953–963, Aug. 2008.
[30] A. Habib, M. Ghanma, M. Morgan, and R. Al-Ruzouq, "Photogrammetric and LiDAR data registration using linear features," *Photogramm. Eng. Remote Sens.*, vol. 71, no. 6, pp. 699–707, Jun. 2005.
[31] A. Habib, S. Shin, C. Kim, and M. Al-Durgham, "Integration of photogrammetric and LiDAR data in a multi-primitive triangulation environment," in *Innovations in 3D Geo Information Systems*. Berlin, Germany: Springer-Verlag, 2006, pt. 2, pp. 29–45.
[32] A. Wong and J. Orchard, "Efficient FFT-accelerated approach to invariant optical-LIDAR registration," *IEEE Trans. Geosci. Remote Sens.*, vol. 46, no. 11, pp. 3917–3925, Nov. 2008.
[33] C. Toth, E. Paska, and D. Brzezinska, "Using pavement markings to support the QA/QC of LiDAR data," *Int. Arch. Photogramm., Remote Sens. Spatial Inf. Sci.*, vol. 36, no. 3/W49B, pp. 173–178, 2007.
[34] H. Kager, "Discrepancies between overlapping laser scanning strips—simultaneous fitting of aerial laser scanner strips," *Int. Arch. Photogramm., Remote Sens. Spatial Inf. Sci.*, vol. 35, no. B1, pp. 555–560, 2004.
[35] Y. Zhang, X. Xiong, and X. Shen, "Automatic registration of urban aerial imagery with airborne LiDAR data," *J. Remote Sens.*, vol. 16, no. 3, pp. 579–595, May 2012.
[36] L. Pilgrim, "Robust estimation applied to surface matching," *ISPRS J. Photogramm. Remote Sens.*, vol. 51, no. 5, pp. 243–257, Oct. 1996.
[37] *Specifications for Aerotriangulation of Digital Aerophotogrammetry*, GB-23236-2009, 2009, Standards Press of China, Beijing, China pp. 5.

Yongjun Zhang was born in 1975. He received the B.S., M.S., and Ph.D. degrees from Wuhan University, Wuhan, China, in 1997, 2000, and 2002, respectively.

He is currently a Professor of photogrammetry and remote sensing with the School of Remote Sensing and Information Engineering, Wuhan University. His research interests include space, aerial and low-attitude photogrammetry, image matching, combined bundle adjustment with multisource data sets, 3-D city reconstruction, and industrial inspection.

Xiaodong Xiong was born in 1987. He received the B.S. degree from Wuhan University, Wuhan, China, in 2009, where he is currently working toward the Ph.D. degree with the School of Remote Sensing and Information Engineering.

His research interests include LiDAR data processing and aerial photogrammetry.

Maoteng Zheng was born in 1987. He received the B.S. degree from Wuhan University, Wuhan, China, in 2009, where he is currently working toward the Ph.D. degree with the School of Remote Sensing and Information Engineering.

His research interests include space and aerial photogrammetry and combined bundle adjustment with multisource data sets.

Xu Huang was born in 1987. He received the B.S. degree from Wuhan University, Wuhan, China, in 2010, where he is currently working toward the Ph.D. degree with the School of Remote Sensing and Information Engineering.

His research interests include computer vision, space/low-attitude photogrammetry, and 3-D reconstruction.